Electron acceleration in a coil target-driven low-β magnetic reconnection simulation

View Online   Export Citation   CrossMark

Jiacheng Yu, [iD] Jiayong Zhong,[a) iD] Yongli Ping, [iD] and Weiming An [iD]

AFFILIATIONS

Department of Astronomy and Institute for Frontiers in Astronomy and Astrophysics, Beijing Normal University,
Beijing 100875, China

[a)]Author to whom correspondence should be addressed: jyzhong@bnu.edu.cn

ABSTRACT

Magnetic reconnection driven by a capacitor coil target is an innovative way to investigate low-β magnetic reconnection in the laboratory, where β is the ratio of particle thermal pressure to magnetic pressure. Low-β magnetic reconnection frequently occurs in the Earth's magnetosphere, where the plasma is characterized by $\beta \lesssim 0.01$. In this paper, we analyze electron acceleration during magnetic reconnection and its effects on the electron energy spectrum via particle-in-cell simulations informed by parameters obtained from experiments. We note that magnetic reconnection starts when the current sheet is down to about three electron inertial lengths. From a quantitative comparison of the different mechanisms underlying the electron acceleration in low-β reconnection driven by coil targets, we find that the electron acceleration is dominated by the betatron mechanism, whereas the parallel electric field plays a cooling role and Fermi acceleration is negligible. The accelerated electrons produce a hardened power-law spectrum with a high-energy bump. We find that injecting electrons into the current sheet is likely to be essential for further acceleration. In addition, we perform simulations for both a double-coil co-directional magnetic field and a single-coil one to eliminate the possibility of direct acceleration of electrons beyond thermal energies by the coil current. The squeeze between the two coil currents can only accelerate electrons inefficiently before reconnection. The simulation results provide insights to guide future experimental improvements in low-β magnetic reconnection driven by capacitor coil targets.

I. INTRODUCTION

Magnetic reconnection, as a fundamental physical process in plasmas, can convert magnetic energy into plasma kinetic energy, accelerate particles to nonthermal energies,[1,2] and change the topology of magnetic fields. Particle acceleration by magnetic reconnection is a common occurrence in magnetic reconnection experiments (MRXs),[3,4] as well as in high-energy astrophysical environments, including solar-terrestrial space,[5,6] solar flares,[7,8] and high-speed jets from pulsars.[9,10] Particle acceleration by magnetic reconnection has been extensively studied and proposed as an explanation for a variety of high-energy astrophysical events.

The study of magnetic reconnection has made considerable progress in recent years,[11] especially in the context of astronomical observations. In addition, magnetic reconnection can now be studied in laboratory experiments, which provide further opportunities for extending the understanding of this phenomenon. There are

two major schemes for driving magnetic reconnection in the laboratory. The first is through the use of magnetically driven systems, which are less subject to disturbances by other unrelated physical processes. The Magnetic Reconnection Experiment (MRX)[12] is a typical device that has been used to perform multiple magnetic reconnection experiments, such as studies of the Hall effect in collisionless magnetic reconnection[13] and of the electron dissipation layer in reconnection.[14] The second scheme uses flow-driven systems, usually based on high-power lasers, and has the merits of a high-density plasma and strong magnetic fields. OMEGA[15] and Shenguang-II,[16] two large laser devices, have been used to perform magnetic reconnection experiments, and promising results have been obtained. Most recent magnetic reconnection experiments[15,17] have involved irradiating a planar target with an intense laser to generate plasma from the target surface. The Biermann self-generated magnetic field around the laser spot then drives magnetic reconnection. This direct-drive method creates a high thermal pressure,

which in turn leads to a high-β ($\beta > 1$) plasma (where β is the ratio of particle thermal pressure to magnetic pressure), whereas low-β ($\beta < 1$) magnetic reconnection is more commonly found in astrophysical plasma environments.

In recent years, capacitor coil targets have been widely employed in the laboratory to produce strong magnetic fields, on the basis of a concept first proposed by Daido *et al.*[18] in 1986. This regime provides a stable and strong external magnetic field, even up to a 1000 T,[19] and such targets are often used to drive low-β magnetic reconnection experiments. A capacitor coil target consists primarily of two target disks connected by a thin copper wire. A laser beam crosses one of the disks to irradiate the other disk. A substantial electric potential difference is thus formed between the two disks as a large number of free electrons are ionized and leave the surface of the rear target disk. A strong magnetic field is induced by the high current in the copper wire, and this enables low-β magnetic reconnection experiment to be performed by using two capacitor coil targets. Pei *et al.*[20] were the first to conduct a low-β magnetic reconnection experiment on Gekko XII using a capacitor coil target and confirmed the feasibility and stability of this experimental scheme. Yuan *et al.*[21] and Chien *et al.*[22] performed detailed experiments on low-β magnetic reconnection with different diagnostics and thereby provided further understanding of this phenomenon. Law *et al.*[23] modeled the emission in the accretion disk corona of black hole systems by means of a novel coil target-driven low-β magnetic reconnection experiment. However, despite these experimental efforts, little work has been done on numerical simulations of low-β magnetic reconnection driven by capacitor coil targets. Such simulations would help develop a more comprehensive understanding of magnetic reconnection experiments and offer positive feedback regarding these experiments.

In this paper, we perform two-dimensional (2D) electromagnetic particle-in-cell (PIC) simulations to investigate low-β magnetic reconnection driven by capacitor coil targets. Our focus is on understanding the acceleration process of nonthermal electrons. To investigate the energization mechanisms of these electrons, we quantify the contributions of different acceleration mechanisms. By tracking a large number of electrons, we investigate the formation of electron power-law spectra and energy spectrum bumps. We also perform simulations of a double-coil co-directional magnetic field and a single-coil one to illustrate the effect of squeeze acceleration on electrons. Section II describes the simulation setup and the various parameters in detail. Section III discusses the acceleration mechanism and power-law energy spectrum of electrons. Section IV presents the conclusions and provides a comprehensive overview of directions for future work.

II. SIMULATION SETUP

The simulation of coil-driven magnetic reconnection was run in the (x, y) plane, with the setup shown schematically in Fig. 1. We used the open-source code SMILEI,[24] which is a fully relativistic electromagnetic PIC code. The initial parameters of the simulation were referenced to the experimental parameters, and some of the parameters in the experiments and simulations are listed in Table I. The ion gyrofrequency Ω_{ci} is proportional to the ion charge Z, and we set $Z = 1$ to save computational resources. We performed two simulations using the different ionization degrees estimated by Chien
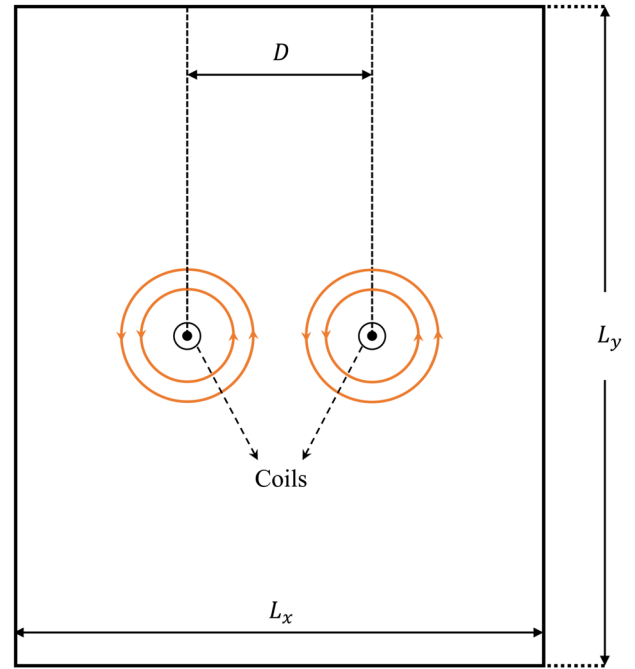

FIG. 1. Schematic of simulation setup. The magnetic field lines are shown in orange.

TABLE I. Experimental[20] and simulation parameters, in normalized units.

Parameter	Expt.	Simulation
Ion mass m_i/m_e	107 767	400
Ion charge Z	28	1
Temperature $T/m_e c^2$	0.0002	0.001
Coil radius r_c/d_i	0.15	0.15
c/v_A	398	13.4
Plasma β	0.016	0.082
Current rise time $\Omega_{ci} t_{\text{rise}}$	2.285	1.14
Coil separation distance D/d_i	2.13	2.13
Ion inertial length d_i/d_e	11.7	20

et al.[25] and Yuan *et al.*[26] to ensure that the choice of ionization degree did not affect our conclusions. The results of these two simulations were indeed consistent with our conclusions. The relevant figures are available in the supplementary material. We determined the initial parameters in the simulation by the ion inertia length, and all parameters were in normalized units. The two coil domains simulated the electric current inside the copper wire and continuously produced an electromagnetic wave that could interact with the particles, but the particles did not affect the coil current. The electric current[27,28] in a coil was described by $I_0(t/2t_{\text{rise}} + 0.5)$ if $t < t_{\text{rise}}$ and by $I_0(1.05 - 0.05t/t_{\text{rise}})$ if $t > t_{\text{rise}}$, where $I_0 = 37.5$ kA, and the current increased from $0.5I_0$. The plasma was initialized with a uniform distribution, and the number densities of particles were $n_i = n_e = n_0$. The simulation domain size was $L_x \times L_y = 6.08d_i \times 7.6d_i$, and the

grid cell size was $\Delta x = \Delta y \approx 0.005 d_i = 0.1 d_e$, where d_i and d_e are the inertial lengths of the ion and electron, respectively. The simulation domain had 5.2×10^8 pseudoparticles, with 128 electrons and ions per grid cell. $\Omega_{ci} = ZeB_0/m_i c$ is the ion gyrofrequency, and the simulation timestep was $\Delta t \approx 2.6 \times 10^{-5} \Omega_{ci}^{-1} \approx 0.066 \omega_{pe}^{-1}$, where ω_{pe} is the electron plasma frequency. The external magnetic field was generated by the coil current and governed by Ampère's law $\partial \mathbf{E}/\partial t = \nabla \times \mathbf{B} - \mathbf{J}$ and Faraday's law $\partial \mathbf{B}/\partial t = -\nabla \times \mathbf{E}$. B_0 represents the magnetic field strength at the center point $(60.8 d_e, 76 d_e)$ when the coil current was at its maximum value, where $B_0 = 50$ T. We adopted absorbing boundary conditions for the electromagnetic field and open boundary conditions for the particles in the simulation.

III. SIMULATION RESULTS

The two plasma bubbles shown in Fig. 2 developed around the coil regions owing to the strong magnetic field generated by the coil current, which is consistent with experimental results.[29] The density measured in the experiment was that of the plasma near the coil, including various plasma sources. Therefore, we used the density values from the experiment as the initial plasma number densities of the simulation. Magnetic flux piles up inside the diffusion region between the two expanding bubbles. Then, the electrons decouple from the magnetic field and form a thin current sheet between the coils. The current sheet thins down to a thickness of $3 d_e$. Magnetic reconnection then occurs, with the reconnection electric field being enhanced immediately, and substantial magnetic energy is released to accelerate the particles. The accelerated particles move quickly toward the outflow region and then cool down. Figure 3(a) shows the oscillation of the electron energy spectral profile in the period $\Omega_{ci} t = 0.98$–3.54. We note that the electron energy spectrum in this period shows a small periodic evolution between being hardened and softened. During the expansion phase of the plasma bubble, some electrons enter the strong-field region ($E_Z/v_A B_0 > 0.3$), i.e., the edge region around the plasma bubble. These electrons are accelerated to energies above $40 \varepsilon_{th}$ (where ε_{th} is the initial thermal energy of the electrons), and these electrons correspond to the nonthermal component of the electron energy spectrum. The power-law spectral index varies between -4.5 and -3 owing to the electron acceleration at the bubble edge and the electron deceleration after leaving the strong-field region. Some accelerated electrons propagate farther away from the strong-field region, and their energy decreases quickly

to $\sim 4 \varepsilon_{th}$. The particle cooling process corresponds to the change in the energy spectrum. As discussed previously, the periodic oscillation of the energy spectrum before reconnection is related to two factors: particle acceleration by the strong field at the plasma bubble edge and the cooling of particles after leaving the strong-field region. Subsequently, we will study the formation of the electron energy spectrum during magnetic reconnection.

Figure 3(b) shows the evolution of the electron energy spectrum during magnetic reconnection, and it can be seen that a high-energy bump appears in the spectrum at $\Omega_{ci} t \sim 5.5$. During reconnection, this bump keeps moving toward the high-energy end, and the spectral index of the electron energy spectrum increases. After the energetic electrons quickly enter the outflow region and cool down, the electron spectrum softens to $p \sim -3$, and the high-energy bump disappears. We now further analyze the formation of the high-energy bump. Electrons in different energy ranges are located at different positions, as shown in Fig. 4(a), where the background is the reconnection electric field. It should be noted that we only tracked the trajectories of $\sim 2 \times 10^5$ electrons. The energetic electrons in the energy range of $100 \leq \varepsilon/\varepsilon_{th}$ are located primarily in the diffusion region of the strong reconnection electric field. The electrons with energy in the range $20 \leq \varepsilon/\varepsilon_{th} \leq 100$ are focused on the outer edge of the diffusion region, while those with energy in the range $9 \leq \varepsilon/\varepsilon_{th} \leq 20$ are mainly located in the transition region between the diffusion region and the outflow region. The features of the distribution of electrons with different energies suggest that the electrons can be effectively accelerated in the current sheet and rapidly decelerate after entering the outflow region. The time evolutions of the reconnection electric field E_Z and the electron kinetic energy shown in Fig. 4 verify the previous result. The electrons accelerated at the bubble edge lead to the creation of a nonthermal component of the energy spectrum before reconnection. Some of these electrons then enter the current sheet to be further accelerated. When reconnection occurs, the electrons in the diffusion region are suddenly accelerated to high energy by the enhanced reconnection electric field, as shown in Figs. 4(b) and 4(d). This further hardens the electron energy spectrum and leads to the formation of a high-energy bump, as shown in Fig. 3(b). Thus, there is a close connection between the electron acceleration in the diffusion region and the profile of the electron energy spectrum. Under different plasma conditions, the process of electron acceleration in the diffusion region is
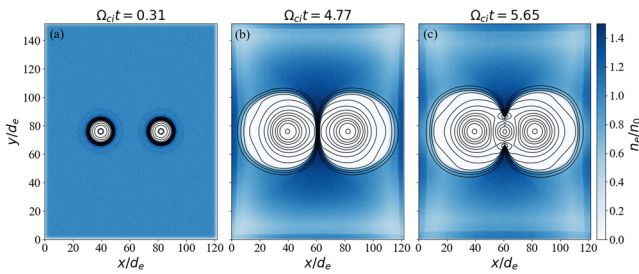

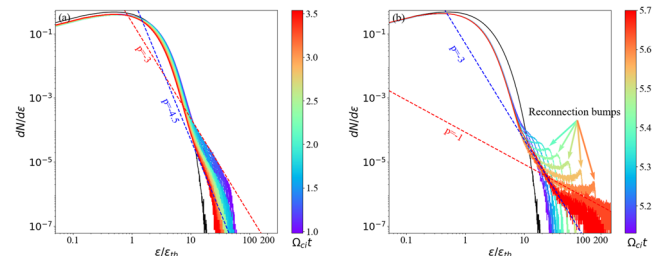**FIG. 2.** Electron number density plots at different time points. The magnetic field lines are shown in black.

FIG. 3. Electron energy spectra at times (a) $\Omega_{ci} t = 0.98$–3.54 and (b) $\Omega_{ci} t = 5.13$–5.70. The dashed lines show the fitted spectral indices, and the black curves are the initial electron energy spectra. The different colors indicate the spectrum at different time points.
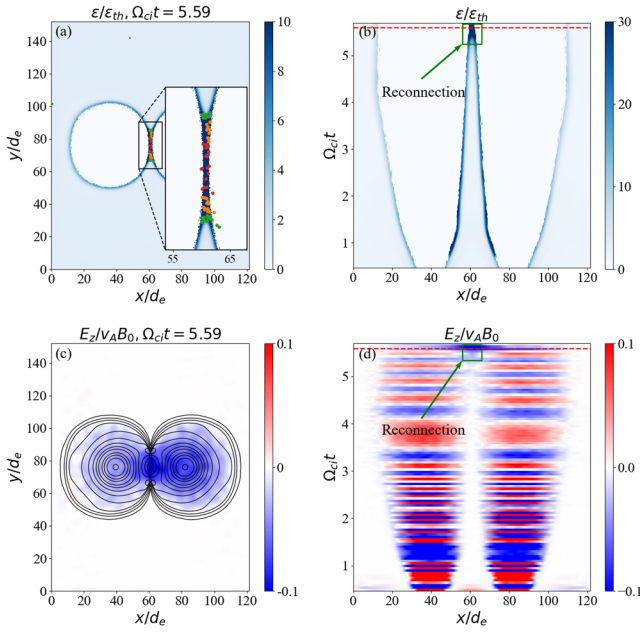
FIG. 4. (a) Electron kinetic energy at $\Omega_{ci}t = 5.59$. The red, orange, and green points represent electrons in the energy ranges $100 \leq \varepsilon/\varepsilon_{th}$, $20 \leq \varepsilon/\varepsilon_{th} \leq 100$, and $9 \leq \varepsilon/\varepsilon_{th} \leq 20$, respectively. (b) and (d) Temporal evolutions of the electron kinetic energy ε and the reconnected electric field E_Z, respectively, along x between $72 \leq y/d_e \leq 80$. The red dashed line marks the time point $\Omega_{ci}t = 5.59$. (c) Reconnection electric field E_Z. The magnetic field lines are shown in black.

not the same.[30,31] Therefore, it is essential to investigate the electron acceleration in the diffusion region. The sign of E_Z keeps changing throughout the simulation, as shown in Fig. 4(d). At the initial moment, the current rises suddenly from $0.5I_0$ rather than linearly from 0, which could excite an electromagnetic wave. Besides, it takes
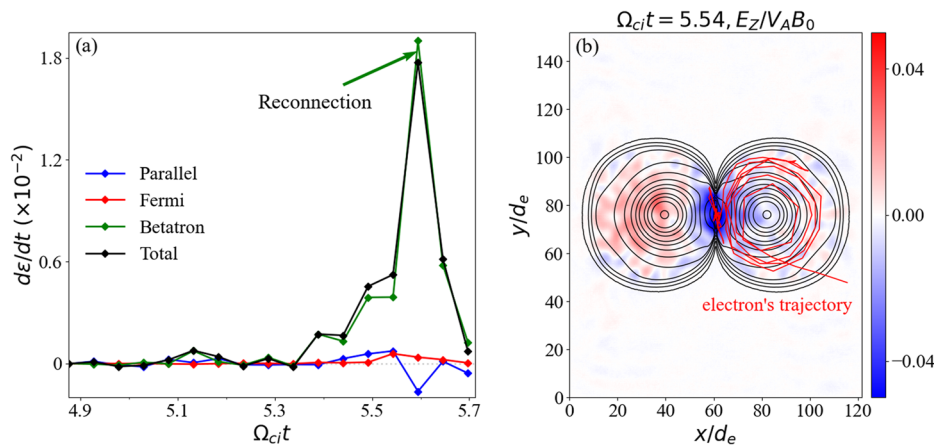
some time for the external magnetic field to respond to the current variation as the coil current varies. These two processes lead to the change in sign of E_Z. Detailed explanations are provided in the supplementary material.

We will calculate the contributions from the various acceleration mechanisms to the electron energy evolution in the current sheet. When the electron gyroradius is smaller than the width of the current sheet, the guiding-center approximation can be employed to analyze the electron acceleration. Calculation of the electron gyroradius $r_e = m_e v_e/eB$ within the current sheet indicates that most electrons have a gyroradius less than the width of the current sheet, with only a few electrons having a gyroradius comparable to that width. Therefore, we choose the guiding-center approximation to investigate the electron acceleration in the simulation.

The guiding-center approximation is described in detail in Refs. 32 and 33. The energy evolution of a single electron in the guiding-center limit is given by

$$\frac{d\varepsilon}{dt} = \frac{\mu \partial B}{\gamma \partial t} + q(v_\parallel \boldsymbol{b} + \boldsymbol{v}_c + \boldsymbol{v}_g) \cdot \boldsymbol{E}, \qquad (1)$$

where

$$\boldsymbol{v}_c = \frac{v_\parallel^2 \boldsymbol{b}}{\Omega_{ce}} \times \boldsymbol{\kappa} \qquad \text{and} \qquad \boldsymbol{v}_g = \frac{v_\perp^2 \boldsymbol{b}}{2\Omega_{ce}} \times \frac{\nabla B}{B}$$

represent the curvature drift term and gradient-B drift term, respectively. $\boldsymbol{b} = \boldsymbol{B}/B$ is the unit vector in the direction of the magnetic field, $v_\parallel = \boldsymbol{v} \cdot \boldsymbol{b}$, $\mu = m_e \gamma^2 v_\perp^2/2B$ is the magnetic moment, γ is the relativistic Lorentz factor, $\Omega_{ce} = qB/\gamma m_e c$ is the electron cyclotron frequency, and $\boldsymbol{\kappa} = \boldsymbol{b} \cdot \nabla \boldsymbol{b}$ is the magnetic curvature. If we consider all the particles in the domain, then Eq. (1) can be rewritten as

$$\frac{dU}{dt} = E_\parallel J_\parallel + \frac{p_\perp}{2B}\left(\frac{\partial B}{\partial t} + \boldsymbol{v}_E \cdot \nabla B\right) + (p_\parallel + n_e m_e v_\parallel^2)\boldsymbol{v}_E \cdot \boldsymbol{\kappa}, \qquad (2)$$

where $\boldsymbol{v}_E = (\boldsymbol{E} \times \boldsymbol{B})/B^2$ is the E-cross-B drift, and $p_\parallel$ and $p_\perp$ are the parallel and perpendicular pressures, respectively. The first term

FIG. 5. (a) Energy evolution over time driven by the parallel electric field (blue), the first-order Fermi acceleration (red), the betatron acceleration (green), and the sum of these three terms (black). The result calculated by summing over all electrons with energy greater than $50\varepsilon_{th}$ corresponds to the bump in the spectrum at $\Omega_{ci}t = 5.54$. (b) Electron trajectory (red line) and reconnection electric field E_Z at $\Omega_{ci}t = 5.54$. The magnetic field lines are shown in black.

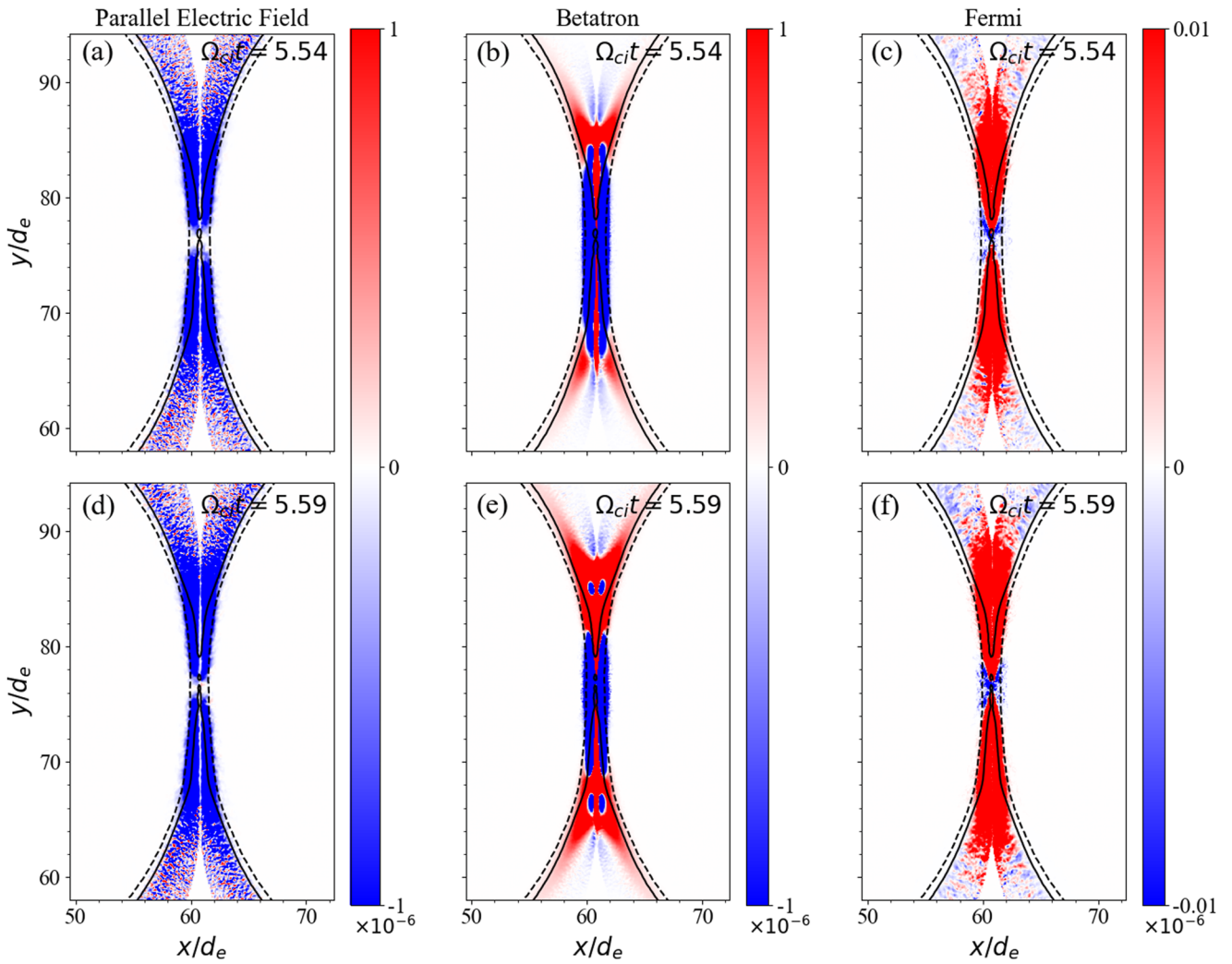**FIG. 6.** (a) and (d) Parallel electric field $E_\parallel J_\parallel$. (b) and (e) Betatron acceleration $(p_\perp/2B)(\partial B/\partial t + \boldsymbol{v_E} \cdot \nabla B)$. (c) and (f) First-order Fermi acceleration $(p_\parallel + n_e m_e v_\parallel^2)\boldsymbol{v_E} \cdot \boldsymbol{\kappa}$. The time point in (a)–(c) is $\Omega_{ci}t = 5.54$, and that in (d)–(f) is $\Omega_{ci}t = 5.59$. The dashed and solid lines represent the contours of electron number density, and the electron number density of the solid lines is an order of magnitude larger than that of the dashed lines.

on the right-hand side of Eq. (2) is the parallel electric field term. The second term represents the contribution of betatron acceleration, which depends on the adiabatic invariant μ and the gradient-B drift. The third term represents the first-order Fermi acceleration. We calculated the contribution of various acceleration mechanisms to a typical energetic electron, and the results are shown in Fig. 5, in which different colored lines represent the evolution of electrons driven by the different acceleration terms. These electrons are picked up from nonthermal electrons with energy greater than $50\varepsilon_{th}$ at $\Omega_{ci}t = 5.54$ and constitute the bump in the electron energy spectrum. The rate of energy change is presented in arbitrary normalized units. The electrons gain energy mainly through the betatron acceleration,

and the first-order Fermi acceleration also makes some contributions to the electron acceleration during magnetic reconnection. Meanwhile, the parallel electric field has a deceleration effect on the electrons. Therefore, the betatron acceleration mechanism is primarily responsible for the appearance of the bump in the electron nonthermal energy spectrum. We investigated the acceleration processes of other nonthermal electrons and came to the same conclusion. The duration of the acceleration is short, owing mainly to the accelerated electrons in the current sheet entering the outflow region and no more particles being injected into the current sheet to maintain the reconnection. Figure 5(b) presents the trajectory of motion of a typical electron. The electrons are first trapped
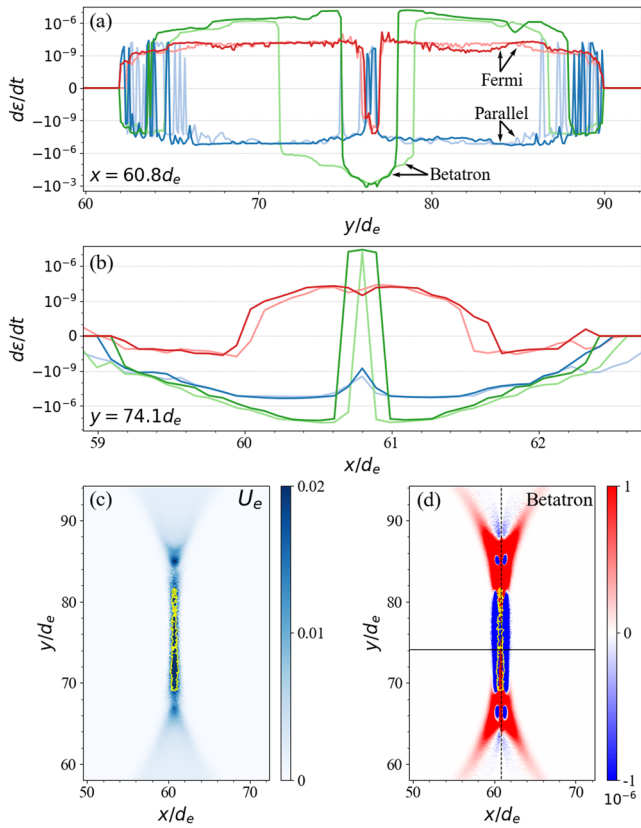
FIG. 7. (a) and (b) Spatial distributions of the different acceleration mechanisms along the dashed ($x = 60.8d_e$) and solid ($y = 74.1d_e$) lines in (d), respectively. Light blue, light green, light red, dark blue, dark green, and dark red correspond to Figs. 6(a)–6(f), respectively. (c) Spatial distribution of electron kinetic energy density U_e at $\Omega_{ci}t = 5.59$. (d) is identical to Fig. 6(e). The yellow lines in (c) and (d) represent the contours of the electron kinetic energy density.

maximum energy that nonthermal electrons can attain. This strong betatron acceleration comes mainly from two effects: one is that the enhanced reconnection electric field leads to the electron vertical velocity $v_\perp$ being larger than the parallel velocity $v_\parallel$, and the other is that there is a large magnetic field gradient within the current sheet. Both of these enable betatron acceleration to dominate the electron acceleration process. The parallel electric field in the current sheet decelerates the electrons. Compared with gradient drift, curvature drift has a weak acceleration effect on the electrons in the current sheet. It should be noted that the magnitude of the acceleration and deceleration driven by the gradient-B drift in Figs. 6(b) and 6(e) is larger by one to two orders of magnitude than that in Figs. 6(c) and 6(f). Figures 7(a) and 7(b) present the spatial distributions of the different acceleration mechanisms, allowing an intuitive comparison of these mechanisms. In Figs. 7(c) and 7(d), the yellow contours show that the regions of high-energy electron concentration and betatron acceleration mostly overlap. Therefore, the betatron acceleration dominates the nonthermal electron acceleration process in the current sheet. In general, the three different mechanisms have both acceleration and deceleration regions in the current sheet. For betatron acceleration, the center is mainly a deceleration region, while the area where electrons are concentrated is an acceleration region. The solid contours in Fig. 6 are an order of magnitude larger than the dashed contours, and so we can infer that the electrons are concentrated within the region enclosed by the solid contours. For Fermi acceleration, there is a small deceleration region in the center, and the other regions are mainly acceleration regions. However, the
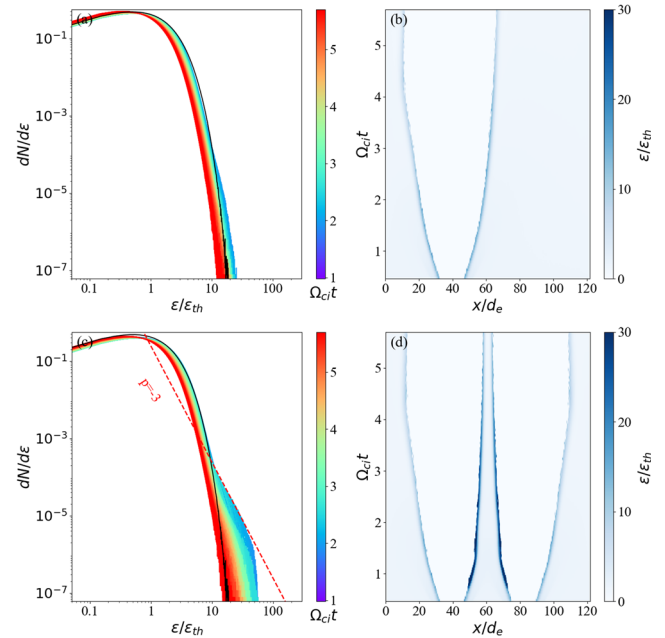
and accelerated by the electromagnetic field at the plasma bubble edge and then injected into the current sheet. We believe that the injection is a necessary preliminary to electron acceleration during magnetic reconnection. Subsequently, the abruptly enhanced reconnection electric field accelerates the electrons in the current sheet. The betatron acceleration mechanism dominates this acceleration process. The electrons eventually enter the outflow region and move along with the relaxation of the reconnected magnetic field or are ejected at high speed.

To directly quantify and compare the contributions of the different terms in Eq. (2), we integrated all electrons over the entire region at time points $\Omega_{ci}t = 5.54$ and 5.59, as shown in Fig. 6. It is evident that the three terms in Eq. (2) have different acceleration and deceleration effects on the electrons in distinct regions. We have confirmed that the choice of boundary conditions does not affect the results for the electron acceleration by performing simulations with different sizes. The acceleration of electrons by the gradient-B drift occurs mainly in the diffusion region and part of the transition region. This acceleration is powerful and directly determines the

FIG. 8. (a) and (c) Electron energy spectra from the single- and double-coil simulations, respectively, at times $\Omega_{ci}t = 0.98$–5.7. The black curves denote the initial electron energy spectrum, and the red dashed line in (c) is a power-law fit. (b) and (d) Time evolutions of the electron kinetic energy ε along x between $72 \leq y/d_e \leq 80$ from the single- and double-coil simulations, respectively.

spatial distribution of the parallel electric field acceleration regions is the opposite to that for Fermi acceleration. Therefore, electrons with different energies undergo different accelerations. This analysis of nonthermal electrons shows that betatron acceleration dominates the acceleration process of most nonthermal electrons in the current sheet.

We also performed two simulations of single-coil (case 2) and double-coil co-directional (case 3) magnetic fields to demonstrate that the acceleration of nonthermal electrons does not depend on the coil current. Figure 8 presents the evolution of the energy spectrum and the electron energy spatial distribution over time in cases 2 and 3. In case 2, the energy of electrons around the current gradually decreases with plasma bubble expansion, and the electron energy spectrum maintains the profile of a Maxwell–Boltzmann distribution. In case 3, coils drive co-directional magnetic fields close to each other. The acceleration of electrons by the ongoing squeeze between currents is not noticeable. This suggests that the nonthermal electrons being accelerated at $\Omega_{ci}t \sim 5.5$ are not driven by the coil current in the two-coil simulation, but result from magnetic reconnection. The two cases further demonstrate that magnetic reconnection can effectively accelerate electrons.

Parallel electric fields are not always very effective for electron acceleration in magnetic reconnection, and sometimes they are negligible. Egedal et al.[34] suggested that parallel electric fields provide electrons with an initial energy boost as they enter the reconnection region, but have no significant effect on the electron acceleration in the current sheet during connection. Li et al.[35] performed a detailed study of low-β magnetic reconnection and concluded that the electron acceleration during reconnection is driven primarily by curvature drift, while the parallel electric field is negligible for electron acceleration. However, the parallel electric field is important for electron acceleration in turbulent magnetic reconnection. Ping et al.[36] confirmed this conclusion through reconnection experiments and PIC simulations. Our paper focuses on a low-β magnetic reconnection driven by the coil target, and we have found that the parallel electric field has a weak deceleration effect on the electrons in the current sheet, which can be neglected compared with the betatron acceleration. Chien et al.[25] directly observed nonthermal electron acceleration in a recent reconnection experiment using a capacitor coil target and combined this observation with PIC simulation results to suggest that the out-of-plane reconnection electric field dominates the electron acceleration. The experimental results of Chien et al.[25] provide direct evidence for the conclusions of this paper.

IV. CONCLUSIONS

We have simulated low-β magnetic reconnection driven by a capacitor coil target using a fully relativistic electromagnetic PIC code. We have estimated the contributions of different acceleration mechanisms of electrons and have analyzed the formation of a spectral bump and a nonthermal component of the electron energy spectrum. As the magnetic flux accumulates in the diffusion region, some electrons are captured by the bubble edge and gain an initial energy boost, which results in the electron power-law spectrum before reconnection. Then, the electrons inside the current sheet experience acceleration dominated by betatron acceleration and deceleration by the parallel electric field during reconnection. The acceleration

of electrons within the current sheet leads to a bump in the electron energy spectrum and further hardens the spectrum. Finally, the electrons are trapped by the relaxation of the reconnected magnetic field when entering the outflow region and cool quickly, which softens the electron energy spectrum. This describes the whole process of electron acceleration in low-β magnetic reconnection driven by a capacitor coil target.

In this work, betatron acceleration dominates the electron acceleration in the current sheet, while the parallel electric field acceleration and the first-order Fermi acceleration are negligible. Some studies[37,38] of magnetic reconnection in the geomagnetic tail have indicated that betatron acceleration is the dominant mechanism of electron acceleration. In the future work, we shall try to explain the electron acceleration in this case by improving the present experiments. We also intend to perform 3D simulations to study the low-β magnetic reconnection driven by a capacitive coil target. The results of such simulations should provide valuable guidance for the application of the results of coil magnetic reconnection experiments to astrophysical magnetic reconnection.

AUTHOR DECLARATIONS

Conflict of Interest

The authors have no conflicts to disclose.

Author Contributions

Jiacheng Yu: Data curation (equal); Formal analysis (equal); Investigation (equal); Methodology (equal); Software (equal); Writing – original draft (equal). **Jiayong Zhong**: Conceptualization (equal); Funding acquisition (equal); Project administration (equal); Supervision (equal); Validation (equal); Writing – review & editing (equal). **Yongli Ping**: Formal analysis (equal); Funding acquisition (equal); Methodology (equal); Software (equal); Supervision (equal); Validation (equal); Writing – review & editing (equal). **Weiming An**: Funding acquisition (equal); Software (equal); Supervision (equal); Writing – review & editing (equal).

DATA AVAILABILITY

The data that support the findings of this study are available from the corresponding author upon reasonable request.
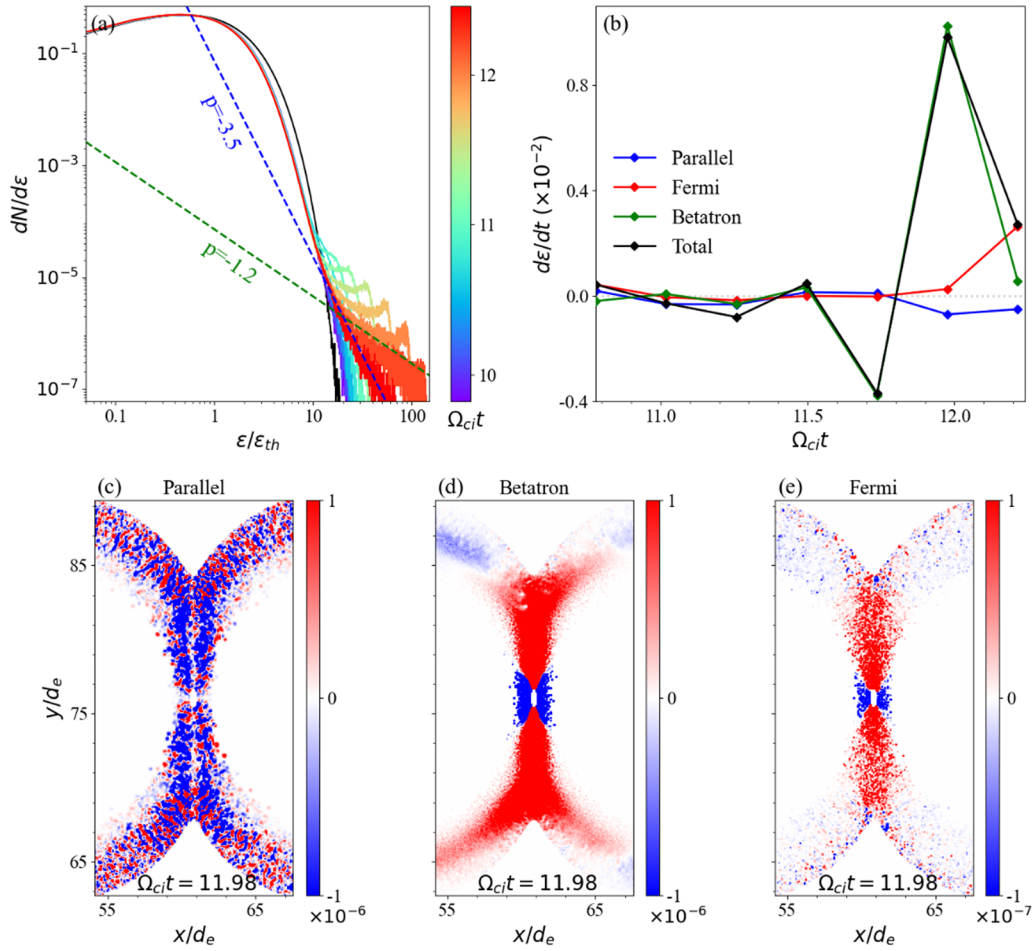
FIG. 9. These results correspond to the ionic charge Z = 6. (a) The variation of the electron energy spectrum containing the high-energy bump during reconnection. The dashed line represents the fitted power-law line. (b) The contribution of each acceleration term to the non-thermal electrons. (c)–(e) Show the spatial distribution of the different acceleration terms.

APPENDIX A: THE DIFFERENT PARAMETERS

We performed two simulations with reference to the parameters of Yuan *et al.*[26] and Chien *et al.*,[25] respectively, and the results as shown in Figs. 9 and 10. The relevant parameters for both simulations are given in Tables II and III. The electron energy spectrum in all three simulations has a bump, but the spectral indices are slightly different. The differences in the non-thermal spectral index of the electrons in these simulations are within the error bars. Coil radius, coil separation, and current rise time may all contribute to the small variations in the spectral index. The exact reasons need to be investigated by further simulations. Figures 9(c)–9(e) and 10(c)–10(e) show a similar spatial distribution as in Fig. 6, and the acceleration curves for all three simulations indicate that the contribution of the betatron acceleration is the largest. These results support the previous conclusion that the betatron mechanism is the dominant mechanism for electron acceleration during magnetic reconnection.

APPENDIX B: THE SIGN CHANGE OF E_Z INSIDE THE PLASMA BUBBLE

In this section, we will explain the asymmetry and the sign change of E_Z in Fig. 4(d) using the higher time resolution simulation. Time-dependent currents can generate time-dependent magnetic fields through Ampere's law $\nabla \times \boldsymbol{B} = \mu_0 \boldsymbol{J} + \partial \boldsymbol{D}/\partial t$. Then, the time-dependent electric field is induced through Faraday's law $\nabla \times \boldsymbol{E} = -\partial \boldsymbol{B}/\partial t$. Here, we only care about the Z component of Ampere's law in normalized: $dE_z/dt = (\partial B_y/\partial x - \partial B_x/\partial y) - J_z$. The external coil current starts to increasing suddenly from $0.5I_0$ rather than linearly from 0. That's why electromagnetic waves are excited at the initial time. We can tell the variation of E_z by $dE_z/dt = (\partial B_y/\partial x - \partial B_x/\partial y) - J_z$, and the magnetic field around the current is unformed when computing this equation for the first time. Therefore, it is reasonable to simplify it to $dE_z/dt = -J_z$. It means that we obtain an E_z with a large value. The large E_z,
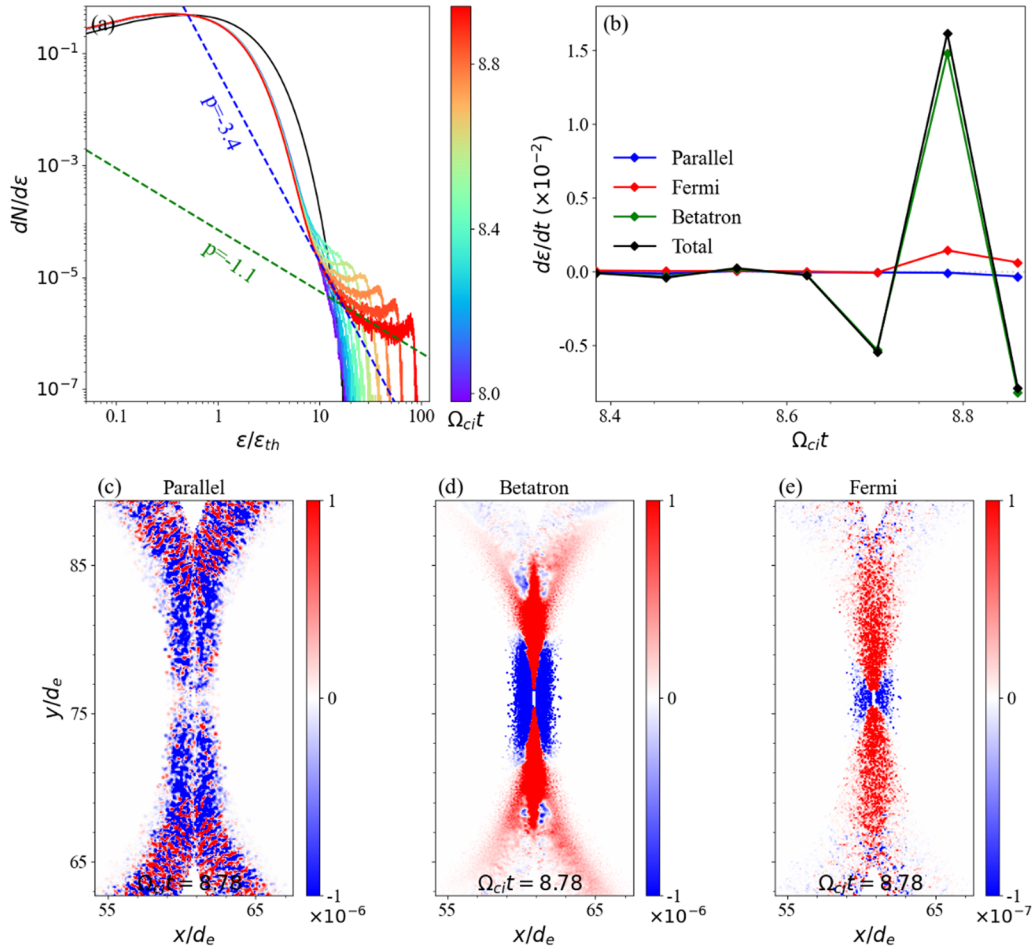
FIG. 10. These results correspond to the ionic charge $Z = 18$. (a) The variation of the electron energy spectrum containing the high-energy bump during reconnection. The dashed line represents the fitted power-law line. (b) The contribution of each acceleration term to the non-thermal electrons. (c)–(e) Show the spatial distribution of the different acceleration terms.

in turn, produces a large B_x and B_y when solving the equations $dB_x/dt = -\partial E_z/\partial y$ and $dB_y/dt = \partial E_z/\partial x$. The initial wave gradually decays as it propagates, and the decay time depends on the strength of the initial wave (in other words, the initial value of J_z). That is

why the spatial field is an oscillating structure in the early times, while there are no significant oscillations in the later times. To further investigate the effect of the initial current, we performed a short simulation [Figs. 11(b) and 11(d)] where the current increases from

TABLE II. Experimental parameters ($Z = 6$) and simulation parameters.

Parameters	Experiment	Simulation
Ion mass m_i/m_e	107 767	400
Ion charge Z	6	1
Temperature $T/m_e c^2$	0.0002	0.001
Coils radius r_c/d_i	0.07	0.07
c/v_A	861	13.4
Plasma β	0.075	0.082
Current rise time $\Omega_{ci} t_{rise}$	10.66	5.33
Coils separation distance D/d_i	0.99	0.99
Ion inertia length d_i/d_e	25.3	20

TABLE III. Experimental parameters ($Z = 18$) and simulation parameters.

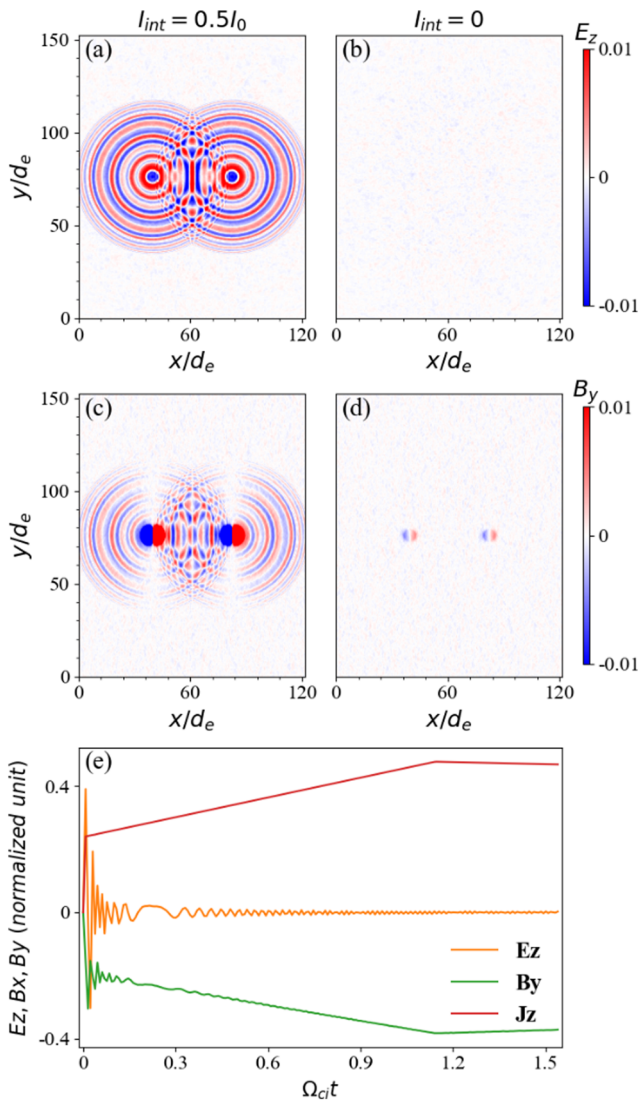| Parameters	Experiment	Simulation
Ion mass m_i/m_e	107 767	400
Ion charge Z	18	1
Temperature $T/m_e c^2$	0.0002	0.001
Coils radius r_c/d_i	0.12	0.12
c/v_A	497	13.4
Plasma β	0.025	0.082
Current rise time $\Omega_{ci} t_{rise}$	3.554	1.78
Coils separation distance D/d_i	1.71	1.71
Ion inertia length d_i/d_e	14.6	20

FIG. 11. Different simulations of E_Z and B_y at $\Omega_{ci}t = 0.015$, where I_{int} is the electric current at $t = 0$. (a), (c), (b) and (d) Correspond to two simulations where the values of I_{int} are $0.5I_0$ and 0, respectively. (e) Shows the variation of the electromagnetic field around the coil with time in the simulation, where the current increases from $0.5I_0$.

FIG. 12. (a) and (c) Show the electric field E_Z at different times. (b) and (d) Is the change rate of the electric field E_Z at different times. The curves in (e) represent the change of integral $E_{dt} = \iint (dE_z/dt)dS/S$ with time in the circles drawn in (c) and (d). For example, the solid green line in (e) shows the result obtained in the solid green ring in (c), and the other curves are similar.

0 instead of $0.5I_0$. Figure 11 shows that the initial waves decayed before $\Omega_{ci}t = 0.015$ in the simulation, where the current increases from 0. The decay process is hard to record because the decay time is smaller than the time step of the simulation.

When the plasma number density around the plasma bubble is high enough, the plasma can screen out electromagnetic fields. The electric field E_Z inside the plasma bubble gradually develops into an irregular structure like Fig. 12(d). There are some specific regions within the bubble where E_Z will increase or decrease, depending on whether the calculated value of dE_z/dt is positive or negative. We can measure the change in E_Z 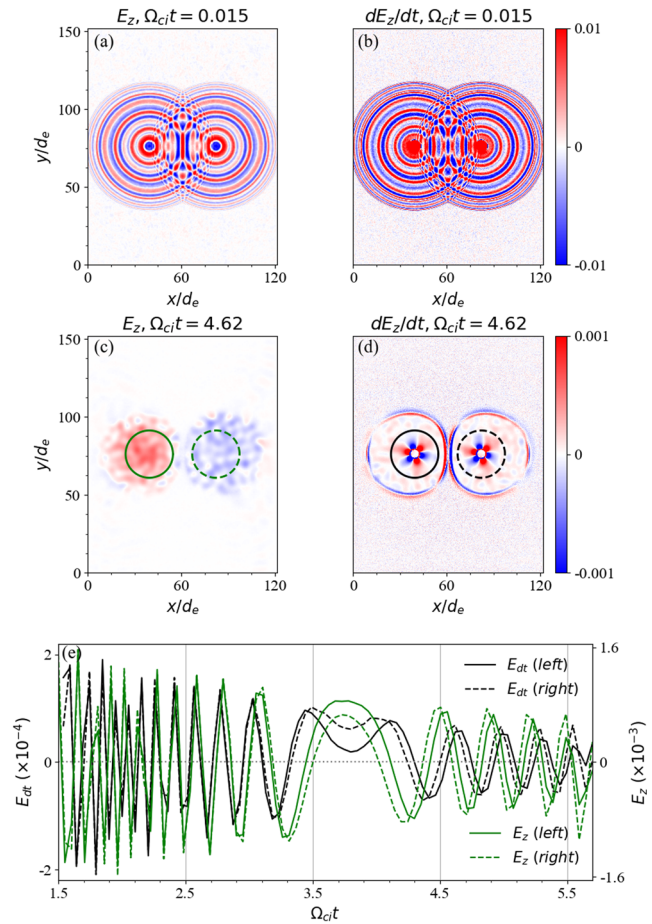by integrating over the dE_z/dt inside the plasma bubble. Figure 12(e) shows the calculation, with the integration region being the circular region in Figs. 12(c) and 12(d). There is a tiny difference in the dE_z/dt between the two plasma bubbles, which results in a difference between the oscillation phases of E_Z inside plasma bubbles. This results in E_Z within the two bubbles having opposite signs for the period when E_Z varies through 0. This is why the E_Z in the two plasma bubbles has an asymmetry similar to Fig. 5(b).

REFERENCES

[1] E. N. Parker, "Sweet's mechanism for merging magnetic fields in conducting fluids," J. Geophys. Res. **62**, 509–520, https://doi.org/10.1029/jz062i004p00509 (1957).

[2] M. Hoshino, T. Mukai, T. Terasawa, and I. Shinohara, "Suprathermal electron acceleration in magnetic reconnection," J. Geophys. Res. **106**, 25979–25997, https://doi.org/10.1029/2001ja900052 (2001).

[3] Y. Ren, M. Yamada, H. Ji, S. P. Gerhardt, and R. Kulsrud, "Identification of the electron-diffusion region during magnetic reconnection in a laboratory plasma," Phys. Rev. Lett. **101**, 085003 (2008).

[4] P. V. Savrukhin, "Generation of suprathermal electrons during magnetic reconnection at the sawtooth crash and disruption instability in the T-10 tokamak," Phys. Rev. Lett. **86**, 3036–3039 (2001).

[5] J. R. Wygant, C. A. Cattell, R. Lysak, Y. Song, J. Dombeck, J. McFadden, F. S. Mozer, C. W. Carlson, G. Parks, E. A. Lucek, A. Balogh, M. Andre, H. Reme, M. Hesse, and C. Mouikis, "Cluster observations of an intense normal component of the electric field at a thin reconnecting current sheet in the tail and its role in the shock-like acceleration of the ion fluid into the separatrix region: Electric fields at the reconnection region," J. Geophys. Res. **110**, A09206, https://doi.org/10.1029/2004ja010708 (2005).

[6] M. Øieroset, R. P. Lin, T. D. Phan, D. E. Larson, and S. D. Bale, "Evidence for electron acceleration up to ~300 keV in the magnetic reconnection diffusion region of Earth's magnetotail," Phys. Rev. Lett. **89**, 195001 (2002).

[7] A. G. Emslie, "Energy partition in two solar flare/CME events," J. Geophys. Res. **109**, A10104, https://doi.org/10.1029/2004ja010571 (2004).

[8] S. Krucker, H. S. Hudson, L. Glesener, S. M. White, S. Masuda, J.-P. Wuelser, and R. P. Lin, "Measurements of the coronal acceleration region of a solar flare," Astrophys. J. **714**, 1108–1119 (2010).

[9] B. Cerutti, D. A. Uzdensky, and M. C. Begelman, "Extreme particle acceleration in magnetic reconnection layers: Application to the gamma-ray flares in the Crab Nebula," Astrophys. J. **746**, 148 (2012).

[10] L. Sironi and A. Spitkovsky, "Relativistic reconnection: An efficient source of non-thermal particles," Astrophys. J. **783**, L21 (2014).

[11] H. Ji, W. Daughton, J. Jara-Almonte, A. Le, A. Stanier, and J. Yoo, "Magnetic reconnection in the era of exascale computing and multiscale experiments," Nat. Rev. Phys. **4**, 263 (2022); arXiv:2202.09004.

[12] M. Yamada, H. Ji, S. Hsu, T. Carter, R. Kulsrud, N. Bretz, F. Jobes, Y. Ono, and F. Perkins, "Study of driven magnetic reconnection in a laboratory plasma," Phys. Plasmas **4**, 1936 (1997).

[13] Y. Ren, M. Yamada, S. Gerhardt, H. Ji, R. Kulsrud, and A. Kuritsyn, "Experimental verification of the Hall effect during magnetic reconnection in a laboratory plasma," Phys. Rev. Lett. **95**, 055003 (2005).

[14] H. Ji, Y. Ren, M. Yamada, S. Dorfman, W. Daughton, and S. P. Gerhardt, "New insights into dissipation in the electron layer during magnetic reconnection," Geophys. Res. Lett. **35**, L13106, https://doi.org/10.1029/2008gl034538 (2008).

[15] P. M. Nilson, L. Willingale, M. C. Kaluza, C. Kamperidis, S. Minardi, M. S. Wei, P. Fernandes, M. Notley, S. Bandyopadhyay, M. Sherlock, R. J. Kingham, M. Tatarakis, Z. Najmudin, W. Rozmus, R. G. Evans, M. G. Haines, A. E. Dangor, and K. Krushelnick, "Magnetic reconnection and plasma dynamics in two-beam laser-solid interactions," Phys. Rev. Lett. **97**, 255001 (2006).

[16] J. Zhong *et al.*, "Modelling loop-top X-ray source and reconnection outflows in solar flares with intense lasers," Nat. Phys. **6**, 984 (2010).

[17] G. Fiksel, W. Fox, A. Bhattacharjee, D. H. Barnak, P.-Y. Chang, K. Germaschewski, S. X. Hu, and P. M. Nilson, "Magnetic reconnection between colliding magnetized laser-produced plasma plumes," Phys. Rev. Lett. **113**, 105003 (2014).

[18] H. Daido, F. Miki, K. Mima, M. Fujita, K. Sawai, H. Fujita, Y. Kitagawa, S. Nakai, and C. Yamanaka, "Generation of a strong magnetic field by an intense CO_2 laser pulse," Phys. Rev. Lett. **56**, 846–849 (1986).

[19] S. Fujioka, Z. Zhang, K. Ishihara, K. Shigemori, Y. Hironaka, T. Johzaki, A. Sunahara, N. Yamamoto, H. Nakashima, T. Watanabe, H. Shiraga, H. Nishimura, and H. Azechi, "Kilotesla magnetic field due to a capacitor-coil target driven by high power laser," Sci. Rep. **3**, 1170 (2013).

[20] X. X. Pei, J. Y. Zhong, Y. Sakawa, Z. Zhang, K. Zhang, H. G. Wei, Y. T. Li, Y. F. Li, B. J. Zhu, T. Sano, Y. Hara, S. Kondo, S. Fujioka, G. Y. Liang, F. L. Wang, and G. Zhao, "Magnetic reconnection driven by Gekko XII lasers with a Helmholtz capacitor-coil target," Phys. Plasmas **23**, 032125 (2016).

[21] X. Yuan, J. Zhong, Z. Zhang, W. Zhou, J. Teng, Y. Li, B. Han, D. Yuan, J. Lin, C. Liu, Y. Li, B. Zhu, H. Wei, G. Liang, W. Hong, S. He, S. Yang, Y. Zhao, Z. Deng, F. Lu, Z. Zhang, B. Zhu, K. Zhou, J. Su, Z. Zhao, Y. Gu, G. Zhao, and J. Zhang, "Low-β magnetic reconnection driven by the intense lasers with a double-turn capacitor-coil," Plasma Phys. Controlled Fusion **60**, 065009 (2018).

[22] A. Chien, L. Gao, H. Ji, X. Yuan, E. G. Blackman, H. Chen, P. C. Efthimion, G. Fiksel, D. H. Froula, K. W. Hill, K. Huang, Q. Lu, J. D. Moody, and P. M. Nilson, "Study of a magnetically driven reconnection platform using ultrafast proton radiography," Phys. Plasmas **26**, 062113 (2019).

[23] K. F. F. Law, Y. Abe, A. Morace, Y. Arikawa, S. Sakata, S. Lee, K. Matsuo, H. Morita, Y. Ochiai, C. Liu, A. Yogo, K. Okamoto, D. Golovin, M. Ehret, T. Ozaki, M. Nakai, Y. Sentoku, J. J. Santos, E. d'Humières, P. Korneev, and S. Fujioka, "Relativistic magnetic reconnection in laser laboratory for testing an emission mechanism of hard-state black hole system," Phys. Rev. E **102**, 033202 (2020).

[24] J. Derouillat, A. Beck, F. Pérez, T. Vinci, M. Chiaramello, A. Grassi, M. Flé, G. Bouchard, I. Plotnikov, N. Aunai, J. Dargent, C. Riconda, and M. Grech, "SMILEI: A collaborative, open-source, multi-purpose particle-in-cell code for plasma simulation," Comput. Phys. Commun. **222**, 351–373 (2018).

[25] A. Chien, L. Gao, S. Zhang, H. Ji, E. G. Blackman, W. Daughton, A. Stanier, A. Le, F. Guo, R. Follett, H. Chen, G. Fiksel, G. Bleotu, R. C. Cauble, S. N. Chen, A. Fazzini, K. Flippo, O. French, D. H. Froula, J. Fuchs, S. Fujioka, S. Kill, S. Klein, C. Kuranz, P. Nilson, A. Rasmus, and R. Takizawa, "Non-thermal electron acceleration from magnetically driven reconnection in a laboratory plasma," Nat. Phys. **19**, 254 (2023).

[26] X. Yuan, C. Zhou, H. Zhang, R. Li, Y. Ping, and J. Zhong, "Particle-in-cell simulations of low-β magnetic reconnection driven by laser interaction with a capacitor–coil target," Chin. Phys. B **32**, 054101 (2023).

[27] G. Fiksel, W. Fox, L. Gao, and H. Ji, "A simple model for estimating a magnetic field in laser-driven coils," Appl. Phys. Lett. **109**, 134103 (2016).

[28] A. Chien, "Particle acceleration due to magnetic reconnection using laser-powered capacitor coils," Ph.D. dissertation (Department of Astrophysical Sciences, Princeton University, 2021).

[29] W. Wang, H. Cai, J. Teng, J. Chen, S. He, L. Shan, F. Lu, Y. Wu, B. Zhang, W. Hong, B. Bi, F. Zhang, D. Liu, F. Xue, B. Li, H. Liu, W. He, J. Jiao, K. Dong, F. Zhang, Y. He, B. Cui, N. Xie, Z. Yuan, C. Tian, X. Wang, K. Zhou, Z. Deng, Z. Zhang, W. Zhou, L. Cao, B. Zhang, S. Zhu, X. He, and Y. Gu, "Efficient production of strong magnetic fields from ultraintense ultrashort laser pulse with capacitor-coil target," Phys. Plasmas **25**, 083111 (2018).

[30] M. Hoshino, "Electron surfing acceleration in magnetic reconnection," J. Geophys. Res. **110**, A10215, https://doi.org/10.1029/2005ja011229 (2005).

[31] D. Ball, L. Sironi, and F. Özel, "Electron and proton acceleration in trans-relativistic magnetic reconnection: Dependence on plasma beta and magnetization," Astrophys. J. **862**, 80 (2018).

[32] J. T. Dahlin, J. F. Drake, and M. Swisdak, "The mechanisms of electron heating and acceleration during magnetic reconnection," Phys. Plasmas **21**, 092304 (2014).

[33] T. G. Northrop, "Adiabatic charged-particle motion," Rev. Geophys. **1**, 283, https://doi.org/10.1029/rg001i003p00283 (1963).

[34] J. Egedal, W. Daughton, A. Le, and A. L. Borg, "Double layer electric fields aiding the production of energetic flat-top distributions and superthermal electrons within magnetic reconnection exhausts," Phys. Plasmas **22**, 101208 (2015).

[35] X. Li, F. Guo, H. Li, and G. Li, "Particle acceleration during magnetic reconnection in a low-beta plasma," Astrophys. J. **843**, 21 (2017).

[36] Y. Ping, J. Zhong, X. Wang, B. Han, W. Sun, Y. Zhang, D. Yuan, C. Xing, J. Wang, Z. Liu, Z. Zhang, B. Qiao, H. Zhang, Y. Li, J. Zhu, G. Zhao, and J. Zhang, "Turbulent magnetic reconnection generated by intense lasers," Nat. Phys. **19**, 263 (2023).

[37] H. S. Fu, Y. V. Khotyaintsev, A. Vaivads, A. Retinò, and M. André, "Energetic electron acceleration by unsteady magnetic reconnection," Nat. Phys. **9**, 426–430 (2013).

[38] Z. H. Zhong, M. Zhou, R. X. Tang, X. H. Deng, D. L. Turner, I. J. Cohen, Y. Pang, H. Y. Man, C. T. Russell, B. L. Giles, W. R. Paterson, Y. Khotyaintsev, and J. L. Burch, "Direct evidence for electron acceleration within ion-scale flux rope," Geophys. Res. Lett. **47**, e2019GL085141, https://doi.org/10.1029/2019gl085141 (2020).